

The prevalence of galaxy overdensities around UV-luminous Lyman α emitters in the Epoch of Reionization

E. Leonova^{1,2,3*}, P. A. Oesch,^{1,4} Y. Qin^{5,6,7}, R. P. Naidu⁸, J. S. B. Wyithe,^{5,6} S. de Barros¹,
R. J. Bouwens,⁹ R. S. Ellis,¹⁰ R. M. Endsley¹¹, A. Hutter¹², G. D. Illingworth,¹³ J. Kerutt,¹ I. Labbé,¹⁴
N. Laporte^{15,16}, D. Magee,¹³ S. J. Mutch,^{5,6} G. W. Roberts-Borsani¹⁷, R. Smit,¹⁸ D. P. Stark,¹¹
M. Stefanon⁹, S. Tacchella¹⁹ and A. Zitrin²⁰

Affiliations are listed at the end of the paper

Accepted 2022 July 5. Received 2022 July 5; in original form 2021 December 13

ABSTRACT

Before the end of the Epoch of Reionization, the Hydrogen in the Universe was predominantly neutral. This leads to a strong attenuation of Ly α lines of $z \gtrsim 6$ galaxies in the intergalactic medium. Nevertheless, Ly α has been detected up to very high redshifts ($z \sim 9$) for several especially UV luminous galaxies. Here, we test to what extent the galaxy's local environment might impact the Ly α transmission of such sources. We present an analysis of dedicated *Hubble Space Telescope* (*HST*) imaging in the CANDELS/EGS field to search for fainter neighbours around three of the most UV luminous and most distant spectroscopically confirmed Ly α emitters: EGS-zs8-1, EGS-zs8-2, and EGSY-z8p7 at $z_{\text{spec}} = 7.73, 7.48, \text{ and } 8.68$, respectively. We combine the multiwavelength *HST* imaging with Spitzer data to reliably select $z \sim 7\text{--}9$ galaxies around the central, UV-luminous sources. In all cases, we find a clear enhancement of neighbouring galaxies compared to the expected number in a blank field (by a factor $\sim 3\text{--}9\times$). Our analysis thus reveals ubiquitous overdensities around luminous Ly α emitting sources in the heart of the cosmic reionization epoch. We show that our results are in excellent agreement with expectations from the DRAGONS simulation, confirming the theoretical prediction that the first ionized bubbles preferentially formed in overdense regions. While three UV luminous galaxies already have spectroscopic redshifts, the majority of the remaining fainter, surrounding sources are yet to be confirmed via spectroscopy. *JWST* follow-up observations of the neighbouring galaxies identified here will thus be needed to confirm their physical association and to map out the ionized regions produced by these sources.

Key words: galaxies: abundances – galaxies: formation – galaxies: groups: general – galaxies: high-redshift – dark ages, reionization, first stars.

1 INTRODUCTION

The Epoch of Reionization (EoR) remains one of the key frontiers of extragalactic studies. Understanding exactly when and how reionization occurred within the first Gyr of cosmic history is a major goal of astronomy over the next decade. While great progress has been made to constrain the overall time frame of reionization through different measurements, including the polarization of the Cosmic Microwave Background (CMB; Planck Collaboration VI 2020), the onset and duration of the EoR are still uncertain (e.g. Greig & Mesinger 2017; Naidu et al. 2020; Bosman et al. 2022; also see Robertson 2021 for a recent review).

An efficient tool used to further constrain the evolution of the neutral fraction at $z > 6$ is the Ly α line emitted by galaxies (so-called Ly α emitters; LAEs). Due to its resonant nature, Ly α is easily scattered and absorbed in the neutral hydrogen in the IGM making LAEs a sensitive probe of the progress of cosmic reionization (e.g. Miralda-Escudé 1998; McQuinn et al. 2007; Dayal, Maselli &

Ferrara 2011; Mason et al. 2018). Indeed, the fraction of continuum-selected galaxies that do show Ly α has been shown to decrease rapidly when entering the neutral phase of the Universe at $z > 6$ (e.g. Fontana et al. 2010; Stark et al. 2010; Schenker et al. 2012; Treu et al. 2013; Pentericci et al. 2014; Hoag et al. 2019; also see Ouchi, Ono & Shibuya 2020 for a recent review).

In stark contrast to this overall decrease of LAE fractions in the EoR are the successful detections and spectroscopic confirmations of particularly luminous, continuum-selected galaxies at $z > 7$. From a UV-luminous sample with $M_{\text{UV}} \sim -22$ mag identified in the CANDELS fields (Roberts-Borsani et al. 2016), all four galaxies were subsequently confirmed spectroscopically through their Ly α line (Oesch et al. 2015; Zitrin et al. 2015; Roberts-Borsani et al. 2016; Stark et al. 2017; Pentericci et al. 2018), and in some cases also through other UV emission lines. These galaxies thus first hinted at a trend of larger Ly α fractions in more luminous galaxies at $z > 7$ compared to fainter sources (see also Ono 2012; Mason et al. 2018). This has subsequently been confirmed with larger statistics (e.g. Jung et al. 2020; Endsley et al. 2021b; Laporte et al. 2021), albeit not all luminous sources at $z > 7$ revealed detectable Ly α .

* E-mail: e.leonova@uva.nl

Several possible explanations for larger detection rates of Ly α in luminous sources have been discussed in the literature. In particular, the sample from Roberts-Borsani et al. (2016) was initially selected through an IRAC excess, which originates from extremely strong [O III] + H β emission lines, with rest-frame equivalent widths in excess of 800 Å. Such strong lines seem to be typical at these redshifts (e.g. Labbé et al. 2013; Smit et al. 2015; De Barros et al. 2019; Endsley et al. 2021a). The strong radiation field required to power such extreme lines might also impact the local environment around these galaxies, increasing the transmission of Ly α (Stark et al. 2017; Endsley et al. 2021b). An additional contribution of ionizing photons could come from an active galactic nucleus (AGN), which might be present in some luminous sources (Tilvi et al. 2016; Laporte et al. 2017; Mainali et al. 2018; Endsley et al. 2021b). Additionally, luminous sources have been observed to show significant velocity offsets between their Ly α lines and the systemic redshifts, likely due to strong outflows (e.g. Erb et al. 2014; Willott et al. 2015; Stark et al. 2017; Hashimoto et al. 2019; Matthee et al. 2020). This would shift the red wing of the Ly α lines further away from the IGM damping wing, further increasing transmission. However, it is still not clear whether this effect is large enough to explain the observed luminosity-dependent evolution of the Ly α fraction over $z = 6-8$ (e.g. Mason et al. 2018).

Another possible explanation for a very high Ly α fraction in luminous sources could be that they are embedded in the most overdense regions. These overdense volumes are expected to reionize first due to the combined emission from both the luminous galaxies and the numerous fainter sources around them (e.g. Barkana & Loeb 2004; Dayal et al. 2009; Pentericci et al. 2011; Endsley et al. 2021b). Indeed, the bright galaxies themselves are most likely unable to emit enough ionizing photons to produce an ionized bubble large enough to allow Ly α photons to escape (e.g. Wyithe & Loeb 2005; Castellano et al. 2022).

Observationally, several galaxy overdensities have now been identified during the EoR both for continuum- and narrow-band-selected galaxies (e.g. Trenti et al. 2012; Ishigaki, Ouchi & Harikane 2016; Hu et al. 2021). In several cases, there is strong evidence for a connection between galaxy overdensities and overlapping ionized bubbles that allow Ly α to be transmitted (e.g. Castellano et al. 2016; Tilvi et al. 2020; Endsley et al. 2021b). In this scenario, reionization starts in the first overdense regions, implying large spatial fluctuations in the ionized fraction and an inhomogeneous topology. This is indeed what is found in cosmological simulations (e.g. Iliiev et al. 2006; Geil et al. 2017; Hutter et al. 2017; Kulkarni et al. 2019; Ocvirk et al. 2020; Gronke et al. 2021; Qin et al. 2022; Smith et al. 2022).

In this paper, we extend the search for overdensities and possible ionized bubbles to very high redshifts. In particular, we obtained dedicated *Hubble Space Telescope* (*HST*) imaging around three of the most distant and UV-luminous Ly α -detected galaxies, in order to search for fainter neighbouring galaxies. In total, we study the environment of four galaxies in the EGS field: three confirmed Ly α emitting sources at $z = 7.5-8.7$, in addition to a photometrically selected galaxy at $z \sim 9$ (see Section 2).

The paper is organized as follows: in Section 2, we present the *HST* and ancillary data sets used. Section 3 focuses on the selection of our galaxy sample, before we quantify the environment around the UV luminous targets in Section 4 and compare our results with simulations in Section 5. Finally, we discuss implications for the Lyman-alpha visibility of luminous reionization-era galaxies in Section 6.

Throughout this paper, we adopt a standard cosmology with $\Omega_m = 0.3$, $\Omega_\Lambda = 0.7$, $h = 0.7$. Magnitudes are given in the AB system.

2 IMAGING DATA

2.1 Ancillary data

The EGS field is one of the five extragalactic fields observed with the Cosmic Assembly Near-infrared Deep Extragalactic Legacy Survey (CANDELS) program (Grogin et al. 2011; Koekemoer et al. 2011). It is centred at (RA, Dec.) = (214.825000, +52.825000) and was originally covered with two-orbit exposures of Advanced Camera for Surveys (ACS) V_{606} , I_{814} and Wide Field Camera 3 (WFC3/IR) J_{125} and H_{160} imaging (0.67 orbits in $F125W$, and 1.33 in $F160W$). The 3D-*HST* survey covers the field with JH_{140} ($F140W$) imaging (Skelton et al. 2014; Momcheva et al. 2016), and a few individual follow-up programs have added targeted Y_{105} ($F105W$) images for a few sources (e.g. Bouwens et al. 2016). Additionally, the field has extensive multiwavelength data from ground-based facilities and was covered with Spitzer's Infrared Array Camera (IRAC) as part of the S-CANDELS program (Ashby et al. 2015). Specifically, we include ground-based K_s -band imaging from the WIRDS survey (Bielby et al. 2012) reaching to 24 mag. Additionally, we have included all available IRAC data over this field, which reaches to ~ 25.4 mag at 3.6 and 4.5 μm and ~ 22.6 mag at 5.8 and 8.0 μm (see Barmby et al. 2008; Ashby et al. 2015; Euclid Collaboration 2022). The total observed area of the EGS field is ~ 200 arcmin². For more information on the ancillary multiwavelength data in this field see e.g. Skelton et al. (2014) and Stefanon et al. (2017).

2.2 Dedicated follow-up of luminous high-redshift sources

The EGS field is especially rich in early galaxies (e.g. Bouwens et al. 2015). It has revealed several particularly luminous high-redshift candidates at $z > 7$ (e.g. Bouwens et al. 2015, 2019; Roberts-Borsani et al. 2016; Finkelstein et al. 2022), three of which have subsequently been confirmed through Ly α emission lines. These are EGS-zs8-1 at $z_{\text{spec}} = 7.7302 \pm 0.0006$ (Oesch et al. 2015; see also Stark et al. 2017; Tilvi et al. 2020), EGS-zs8-2 at $z_{\text{spec}} = 7.4770 \pm 0.0008$ (Roberts-Borsani et al. 2016; Stark et al. 2017), and EGSY-z8p7 at $z_{\text{spec}} = 8.683^{+0.001}_{-0.004}$ (Zitrin et al. 2015; see also Mainali et al. 2018). All of these sources are expected to exhibit strong radiation fields due to high-equivalent width [O III] + H β emission lines identified through their Spitzer/IRAC photometry (Roberts-Borsani et al. 2016). Indeed, highly excited UV lines have been confirmed in the MOSFIRE spectra of EGS-zs8-1 (C III; Stark et al. 2017) and EGSY-z8p7 (N V; Mainali et al. 2018). Especially the detection of the N V line in EGSY-z8p7 points to a non-negligible, possible contribution from an AGN.

While other particularly distant EoR galaxies have been spectroscopically confirmed since the discovery of LAE targets (e.g. Oesch et al. 2016; Hashimoto et al. 2018; Jung et al. 2020; Jiang et al. 2021; Laporte et al. 2021), these sources in the EGS field still rank among the most distant detected Ly α emission lines (see also Larson et al. 2022). For more information on the luminous Ly α sources, see Section 3.1, Tables 1 and 2.

To explore whether these very early Lyman-alpha emitters commonly reside in overdense regions, we have obtained dedicated, additional multicolour *HST* WFC3/IR observations around these three luminous galaxies (GO-15103; De Barros 2017). In particular, we added the missing $F105W$ filter that is necessary to reliably identify $z \sim 7.5-9$ galaxies and measure improved photometric redshifts of fainter galaxies surrounding brighter Ly α emitting galaxies, in addition to deeper $F125W$ and $F160W$ imaging. The program was designed to identify galaxies that are up to an order of

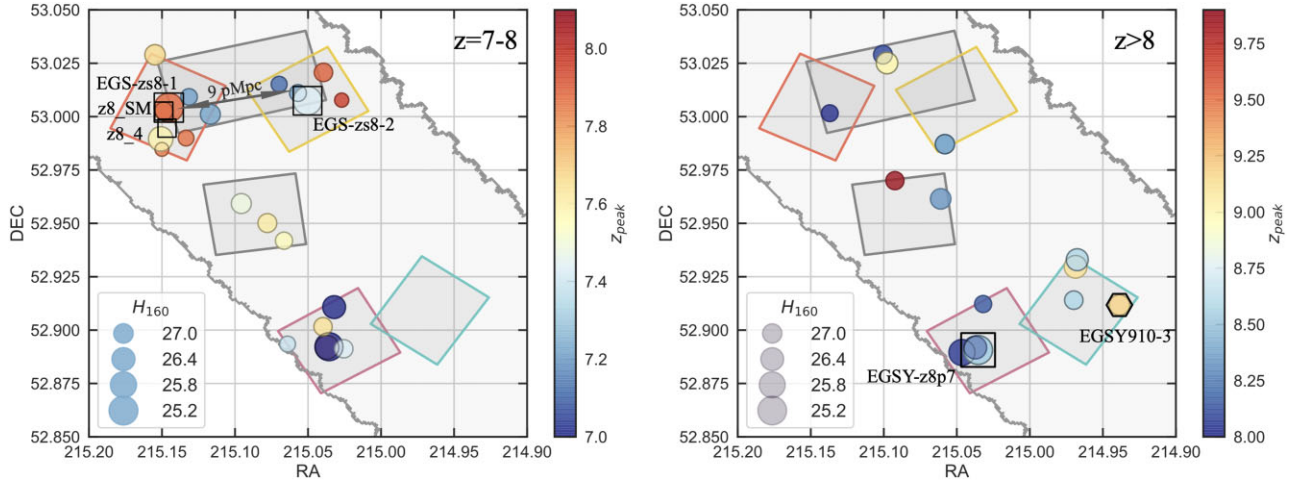


Figure 1. Position of all selected sources in the CANDLES/EGS field centred around our target galaxies. Sources with redshift $7 < z_{\text{phot}} < 8$ are shown in the left-hand panel, while galaxies with $z_{\text{phot}} > 8$ are indicated on the right-hand panel. The fields are shown North up, East left. The light shaded region shows the CANDELS H_{160} coverage. The darker grey areas show fields where $F105W$ imaging is available and that have been included in our search. The three pointings from our own program were centred on EGS-zs8-1 (orange outline), EGS-zs8-2 (yellow), and EGSY-z8p7 (pink). Also highlighted (in green) is the $F105W$ outline around EGS910-3 presented in Bouwens et al. (2016) that we include in our analysis. The black squares correspond to the location of LAEs. The colourbars indicate the photometric redshifts of the sources. The sizes of the circles represent their H_{160} magnitude. Also indicated is the 3D distance of nine physical Mpc between the two $\text{Ly}\alpha$ galaxies at $z \sim 7.6$ on the left.

magnitude less luminous than the main targets, which have $H_{AB} = 25.0\text{--}25.3$ mag. In particular, we obtained five-orbit exposures in three individual pointings centred on each of the three luminous LAEs (two orbits in $F105W$, 1.5 in $F125W$, and 1.5 in $F160W$). When combined with the previous, CANDELS HST imaging our data reach 5σ limits of 27.9 mag in $F105W$, 27.5 mag in $F125W$, and 27.5 mag in $F160W$, respectively.

In addition to our dedicated HST data, we retrieved all the HST ACS and WFC3/IR data available around the EGS sources from the HST archive and combined them into one mosaic as part of the Hubble Legacy Field project (Illingworth et al., in preparation).

2.3 Source detection and multiwavelength photometry

The HST images in different bands were convolved to the same point spread function (PSF); using convolution kernels analogous to the ones made available by the 3D- HST team; Skelton et al. 2014). We then use SEXTRACTOR (Bertin & Arnouts 1996) to detect sources in a combined $F125W + F160W$ image and measure their colours through matched, circular apertures. In particular, we use small apertures with 0.5 arcsec diameter to measure colours, which are then corrected to total fluxes with a median multiplication factor of 1.7 to match the SEXTRACTOR AUTO fluxes in the $F160W$ image.

In order to obtain IRAC photometry in all four channels, we follow the same procedure as described in Stefanon et al. (2021a). To overcome confusion, we subtract contaminating flux of neighbouring galaxies using the Mophongo tool (see e.g. Labbé et al. 2013, 2015), before measuring the IRAC fluxes in 1.8 arcsec diameter apertures and correcting to total fluxes. When the contamination by neighbour is too large for a reliable subtraction, the IRAC fluxes are flagged and ignored in the subsequent spectral energy distribution (SED) fits. We use the same procedure to derive photometry from ground-based K -band images. Overall, we thus obtain 11-band SEDs for all sources ($6\times HST$, K band, and $4\times IRAC$), spanning 0.6 to 8 μm .

3 SAMPLE SELECTION

3.1 Central LAE targets

Our HST observations are centred around three UV luminous galaxies at $z \geq 7.5$ that have been confirmed through $\text{Ly}\alpha$ in the EGS field (see Section 2.2). One of these, EGS-zs8-1, has subsequently been observed through narrow-band observations, from which two fainter LAEs have been identified in its immediate proximity (Tilvi et al. 2020). These latter sources have also been confirmed through $\text{Ly}\alpha$ spectroscopy and they were named z8.SM at $z = 7.767$ and z8.4 at $z = 7.748$. They likely sit in a common, ionized bubble with EGS-zs8-1, since they are only separated by 0.7 to 0.8 physical Mpc (pMpc) from each other and their estimated ionized bubble radii reach 0.5–1.0 pMpc.

Additionally, the 3D distance between the galaxy EGS-zs8-1 and the other UV-luminous, spectroscopically confirmed source EGS-zs8-2 at $z = 7.48$ is only 9.1 pMpc. This distance is smaller than the average bubble radius of $\lesssim 10$ pMpc expected at the end of cosmic reionization (Wyithe & Loeb 2005; Geil et al. 2017), and points at a larger scale overdensity in this field at this redshift. One of the main goals of our follow-up observations was to further characterize this overdensity through fainter sources. Hence, we centred two of our HST pointings around EGS-zs8-1 and EGS-zs8-2, respectively (orange and yellow outlines in Fig. 1).

The last pointing was centred around EGSY-z8p7, one of the most distant known LAEs with $z_{\text{spec}} = 8.683$ (pink outline in Fig. 1). This source has a potential companion at < 10 pMpc: the galaxy EGS910-3 (Bouwens et al. 2016, see also Bouwens et al. 2019). On the sky, these two sources are separated by only 3.7 arcmin. However, the source only has a photometric redshift measurement ($z_{\text{phot}} = 9.0^{+0.5}_{-0.7}$ as derived in Bouwens et al. 2016) and has not been confirmed through spectroscopy so far. Hence, the actual physical separation from EGSY-z8p7 is uncertain. The source EGS910-3 has also been targeted by $F105W$ follow-up observations, which we retrieve from the archive and include in our analysis (see e.g. Fig. A1).

3.2 Selection of neighbouring $z = 7-9$ candidates

3.2.1 Selection criteria

The main goal of our program was to identify fainter sources around the central UV-luminous targets. We thus use the *HST*-detected multiwavelength catalogues described in Section 2.3 to select candidate high-redshift sources. Specifically, we use a combination of detection and non-detection criteria as expected for Lyman break galaxies together with a photometric redshift selection. We only consider sources that are significantly detected in both the *F125W* and *F160W* bands with the following criteria:

$$S/N(J_{125}) > 3 \wedge (S/N)_{\text{det}} > 5 \wedge S/N(H_{160}) > 4, \quad (1)$$

where $(S/N)_{\text{det}}$ corresponds to the signal-to-noise ratio in the combined *F125W* and *F160W* image. These criteria allow us to identify sources down to $H_{160} = 27.7$ mag. Additionally, the sources were required to not be detected in the two optical *HST* filters with: $S/N(V_{606}) < 2 \wedge S/N(I_{814}) < 2$. In selecting these sources, we have only included areas that also have *F105W* imaging coverage, either from our own follow-up program or from archival observations (darker areas in Fig. 1).

Photometric redshifts are then derived for all the sources that pass the above criteria. We use the python version of the publicly available code EAZY¹ (Brammer, van Dokkum & Coppi 2008) which provides the photometric redshift probability distribution function (pdf), $\mathcal{P}(z)$, based on a χ^2 fit of SED models to the observed photometry. Specifically, we use the template set ‘eazy_v1.1’ which includes emission lines. We have also tested other template sets, but have not found large differences. EAZY also accounts for the intergalactic absorption by neutral hydrogen (Madau 1995). The redshifts have been searched over $0.1 \leq z \leq 12$.

Based on the EAZY output we then only include sources that have a best-fitting photometric redshift in our range of interest, depending on the central target sources. For the fields around EGS-zs8-1 and -2, we select galaxies with $z_{\text{phot}} = 7-8$, where the value of z_{phot} is defined as the peak of $\mathcal{P}(z)$. To ensure that these redshifts are reasonably accurate, we exclude galaxies with a photometric redshift pdf that is too wide, i.e. galaxies are required to have $\mathcal{P}(6 \leq z \leq 9) \geq 50$ per cent. For the fields around EGSY-z8p7, we select sources with $z_{\text{phot}} > 8$ that have $\mathcal{P}(z \geq 7) \geq 50$ per cent. In Fig. A1, we illustrate the SEDs and redshift pdfs of the central UV-luminous LAEs and EGS910-3. As can be seen, the photometric redshift determinations of the Ly α sources are in excellent agreement with their spectroscopic redshifts, with a very narrow $\mathcal{P}(z)$. For the last source, we confirm the photometric redshift solution from Bouwens et al. (2016), as we measure a consistent value of $z_{\text{phot}} = 9.18_{-0.55}^{+0.95}$.

3.2.2 Exclusion of dwarf stars

Cool dwarf stars can mimic the colours of high-redshift Lyman break galaxies (e.g. Wilkins, Stanway & Bremer 2014). They can remain undetected in optical bands (in *F606W* and *F814W* filters) and peak in the Near-infrared (NIR). To remove such sources from our catalogues of LBG candidates we use a combination of two different measurements. First, we identify potential unresolved sources using the SEXTRACTOR parameter CLASS_STAR, and second we run EAZY with a set of dwarf star templates fixed at $z = 0$ to compare the χ^2 from both dwarf stars and galaxy templates. The

CLASS_STAR parameter on its own is not reliable, especially at faint magnitudes.

Objects with CLASS_STAR more than 0.6 and χ^2 from star templates less than χ^2 from galaxy template are removed from the catalogues:

$$\text{CLASS_STAR} > 0.6 \wedge \left(\chi_{\text{galaxy}}^2 / \chi_{\text{star}}^2 \right) > 1 \quad (2)$$

In total, only two sources have been removed based on these criteria. Visual inspection of these sources indeed confirmed them to be unresolved, and hence more likely to be stars than high-redshift galaxies.

3.2.3 Final sample

After excluding two likely dwarf stars, our final sample of high-redshift galaxies within the four WFC3/IR pointings around the four UV-luminous central targets consists of 21 sources in total. Their positions are shown in Fig. 1. In the following text, we will discuss the individual environment around the four central sources.

With eight sources, the pointing around EGS-zs8-1 revealed the largest number of high-redshift galaxy candidates at $z = 7-8$ (including the central source itself). The EGS-zs8-2 field resulted in five sources. Note that the spectroscopically confirmed source z8_4 is not included in our photometric sample due to a photometric redshift that was too low. For completeness, we show the galaxy in Fig. 1.

At higher redshifts, the fields around EGSY-z8p7 and EGS910-3 reveal four sources with $z_{\text{phot}} > 8$ each. All these sources are listed in Tables 1 and 2. The photometric redshift distribution functions and stamps for the luminous sources can be found in the appendix in Fig. A1, while the fainter, neighbouring sources are shown in Figs A2 to A5.

4 THE ENVIRONMENT OF UV LUMINOUS GALAXIES

A principle goal of our work is to quantify the environment and possible overdensities of UV luminous sources with Ly α emission at $z > 7$. To do this, we first need to estimate the expected number of galaxies in a given area, which we do based on two different approaches that are described in the following subsections.

4.1 Expected number of galaxies

4.1.1 Based on the UV luminosity function

The first approach to estimate how many galaxies we expect to find within a given area is based on the UV luminosity function (LF) and the galaxy selection efficiency. Following previous literature (e.g. Castellano et al. 2016), we estimate the selection efficiency of our survey by simulating the photometry for a large number of high-redshift galaxies. Specifically, we introduce $> 60\,000$ artificial galaxies with a range of known (input) magnitudes 24–29 mag, colour distribution, and redshifts $6 < z < 10$.

Since high-redshift galaxy selections can be sensitive to the UV colours, we simulate the artificial sample with a colour distribution that matches observations. To do this, we start with a Bruzual & Charlot (2003) template with an age of 100 Myr and a constant star-formation history. Calzetti et al. (2000) dust is then applied following a normal distribution of $E(B - V)$ with a mean of 0.1 and a $\sigma = 0.15$, truncated at zero (following Finkelstein et al. 2022). Nebular continuum and emission lines have been added empirically based on

¹<https://github.com/gbrammer/eazy-py>

Table 1. Table with parameters of all sources with redshift $z \sim 7-8$ identified in the *F105W* footprints around the two LAEs.

ID	RA	Dec.	H ₁₆₀ [mag]	z _{phot}	$\int \mathcal{P}(6 \leq z \leq 9)$	z _{spec}	Separation ^a [arcmin]	References
EGS-zs8-2 group								
EGS-zs8-2	215.0503352	53.0074442	25.25 ± 0.03	7.43 ^{+0.08} _{-0.09}	1.00	7.477	0.0	(1),(3)
EGSY-94562	215.0394433	53.0207175	27.2 ± 0.3	7.90 ^{+0.04} _{-1.90}	0.55	–	0.9	
EGSY-80113	215.056893	53.0110575	27.4 ± 0.2	7.22 ^{+0.02} _{-1.22}	0.50	–	0.3	
EGSY-76521	215.0697905	53.0151445	27.5 ± 0.2	7.12 ^{+0.20} _{-0.93}	0.90	–	0.8	
EGSY-91929	215.0269545	53.0077343	27.7 ± 0.2	7.96 ^{+0.20} _{-0.95}	0.93	–	0.8	
EGS-zs8-1 group								
EGS-zs8-1	215.1453377	53.0042107	25.12 ± 0.04	7.88 ^{+0.06} _{-0.05}	1.00	7.728	0.0	(1),(2),(3),(4)
EGSY-23959	215.1508931	52.9895618	26.1 ± 0.1	7.59 ^{+0.13} _{-0.36}	1.00	–	0.9	
EGSY-46810	215.154764	53.0289543	26.8 ± 0.1	7.67 ^{+0.23} _{-1.67}	0.66	–	1.5	
EGSY-46009	215.1168772	53.0010665	26.9 ± 0.2	7.22 ^{+0.10} _{-1.16}	0.86	–	1.0	
z8_SM	215.1487577	53.0025984	27.2 ± 0.1	7.89 ^{+0.16} _{-0.29}	1.00	7.767	0.2	(4)
EGSY-44464	215.1314765	53.0092156	27.4 ± 0.2	7.21 ^{+0.09} _{-1.21}	0.76	–	0.6	
EGSY-31530	215.1334993	52.9899563	27.5 ± 0.2	7.86 ^{+0.41} _{-1.86}	0.51	–	1.0	
EGSY-21312	215.150041	52.9846593	27.7 ± 0.2	7.85 ^{+0.24} _{-0.70}	0.96	–	1.2	
z8_4*	215.1465376	52.994614	26.8 ± 0.3	6.16 ^{+0.90} _{-0.48}	–	7.748	0.6	(4)

Notes. ^aSeparation from the central luminous source in arcmin.

*z8_4 was not selected in our sample due to a lower photometric redshift.

References: (1) Roberts-Borsani et al. (2016), (2) Oesch et al. (2015), (3) Stark et al. (2017), (4) Tilvi et al. (2020).

Table 2. Table with parameters of all sources with redshift $z \sim 8-9$ identified in the *F105W* footprints around the two $z > 8$ galaxies.

ID	RA	Dec.	H ₁₆₀ [mag]	z _{phot}	$\int \mathcal{P}(z \geq 7)$	z _{spec}	Separation ^a [arcmin]	References
EGSY-z8p7 group								
EGSY-z8p7	215.0354269	52.8906918	25.19 ± 0.03	8.55 ^{+0.14} _{-0.15}	1.00	8.683	0.0	(1),(2),(3),(4)
EGSY-6887*	215.0465028	52.8895178	25.8 ± 0.1	8.05 ^{+0.22} _{-0.54}	0.95	–	0.4	
EGSY-12580 [†]	215.0373571	52.8918284	26.4 ± 0.2	8.07 ^{+0.19} _{-0.29}	0.99	–	0.1	
EGSY-27727	215.031966	52.9122172	27.3 ± 0.2	8.15 ^{+0.79} _{-1.78}	0.75	–	1.3	
EGS910-3 group								
EGS910-3	214.9386673	52.911176	26.8 ± 0.2	9.18 ^{+0.95} _{-0.55}	0.92	–	0.0	(2),(3)
EGSY-66990	214.968693	52.9296537	26.4 ± 0.2	9.12 ^{+0.14} _{-1.08}	0.95	–	1.5	
EGSY-69674	214.9675507	52.932962	26.6 ± 0.1	8.60 ^{+0.25} _{-0.44}	0.99	–	1.6	(3),(4)
EGSY-56680	214.9699133	52.9140338	27.2 ± 0.1	8.60 ^{+0.14} _{-2.60}	0.70	–	1.1	

Notes. ^aSeparation from the central luminous source in arcmin.

*This source lies very close to a clumpy foreground galaxy, which could affect its photometric measurements.

[†]This source has a close companion, which was excluded from our list due to its photometric redshift just below the cut-off of our selection.

References: (1) Zitrin et al. (2015), (2) Bouwens et al. (2016), (3) Bouwens et al. (2019), (4) Finkelstein et al. (2022)

the total number of ionizing photons produced by the underlying SED and using line ratios from Anders & Fritze-v. Alvensleben (2003). Finally, IGM attenuation is applied according to the prescription of Madau (1995) and set by the simulated redshift of each galaxy. For $z > 7$, this essentially corresponds to a sharp break at the redshifted Ly α line. The final SEDs are then convolved with all the *HST* and Spitzer IRAC transmission curves to derive the expected, intrinsic fluxes. These are subsequently disturbed using Gaussian flux uncertainties, based on the median flux σ as measured for real sources in our *HST* footprints in the respective filters.

We then perform the same analysis as for the real catalogue. First, the detection and optical non-detection criteria are applied and the EAZY photometric redshifts and pdfs are computed as was done for the real galaxies. This allows us to compute the completeness in bins of input magnitude M and redshift z as the ratio between the number

of galaxies that pass our selection and the number of input galaxies in the respective bin:

$$\mathcal{P}(M, z) = \frac{N_{\text{sel}}}{N_{\text{in}}}. \quad (3)$$

Now that we have the selection efficiency, it is straightforward to compute the expected number of galaxy detections based on the empirical UV LF. To do this, we use the Schechter parameter evolution derived in Bouwens et al. (2021) at $z \sim 2-10$:

$$\begin{cases} M_{\text{UV}}^* = -21.03 - 0.04(z - 6) \\ \phi^*/\text{Mpc}^{-3} = 0.4 \times 10^{-3} \times 10^{-0.33(z-6) - 0.24(z-6)^2} \\ \alpha = -1.94 - 0.11(z - 6) \end{cases} \quad (4)$$

The expected number of detections can then be derived by multiplying the UV LF with the probability that a galaxy of absolute

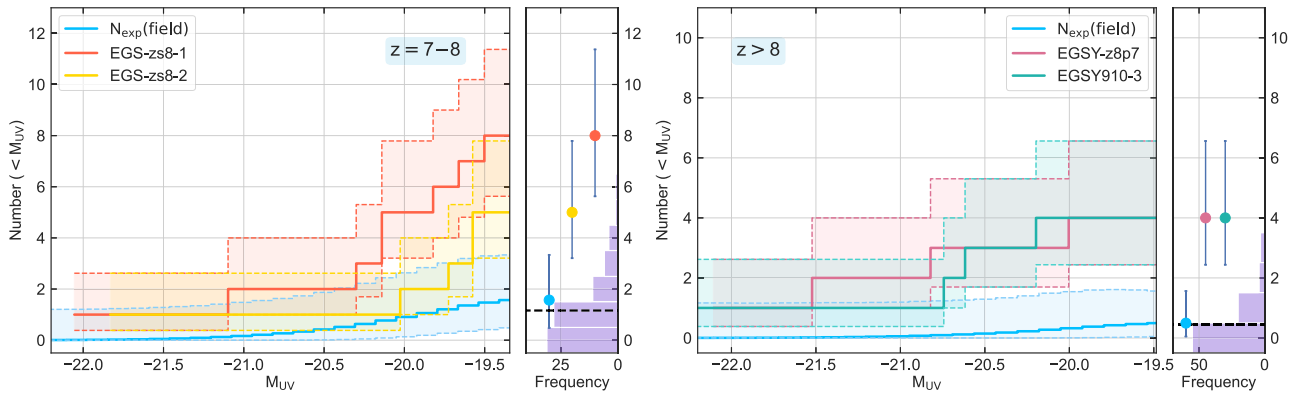


Figure 2. The cumulative number of the sources within an area of 4.5 arcmin^2 at $z = 7-8$ (left-hand panels) and $z > 8$ (right-hand panels). The left-hand panels show the cumulative numbers as a function of absolute magnitude. The blue line corresponds to the expected number based on the UV LF and our selection function, while the coloured lines correspond to the actual numbers of galaxies that we have identified in the *HST* data in the different fields (orange for EGS-zs8-1; yellow for EGS-zs8-2; pink for EGSY-8p7; green for EGS910-3). The shaded regions correspond to the 16th to 84th percentile uncertainties for a Poisson distribution convolved with cosmic variance (see the text for details). The right-hand panels show the total number of sources selected down to our magnitude limits using the same colours as for the cumulative histograms, with the points offset horizontally for clarity. Additionally, the purple histograms show the distribution of high-redshift galaxies selected in 82 independent 4.5 arcmin^2 cells in the GOODS-S and GOODS-N fields, using the same selection criteria as for our *HST* data in the EGS field (see Section 4.1.2). The dashed black line corresponds to the mean in the GOODS fields, which is consistent with the mean expected number from the UV LF (blue). As is evident from these figures, the environment around all four UV luminous sources are overdense relative to the general field. The enhancement ranges from $3 \times$ to $9 \times$, which corresponds to a $2-3\sigma$ result for each individual case (see the text for details).

magnitude M at redshift z is selected, $\mathcal{P}(M, z)$, within the same area as used for real sources.

$$N_{\text{exp}} = \int \Omega \frac{dV_{\text{com}}}{dz} dz \int \phi(M) \mathcal{P}(M, z) dM, \quad (5)$$

where $\phi(M)$ is the UV LF, Ω is the survey area for each *HST* field, i.e. 4.5 arcmin^2 for a WFC3/IR pointing.

For the $z \sim 7-8$ galaxy samples around EGS-zs8-1 and -2, we derive an expected number of 1.57 galaxies per WFC3/IR pointing down to our detection limit of 27.7 mag (see Fig. 2). For the $z \sim 8-9$ samples, the expected number is only 0.45 sources per WFC3/IR field.

4.1.2 Empirical approach

Another way to determine whether a given *HST* field might be overdense can be derived empirically using the number counts from another field that is as deep or deeper than the field in question. We can thus use the CANDELS/GOODS-North and CANDELS/GOODS-South fields with an area of $\sim 170 \text{ arcmin}^2$ each, from which high-redshift galaxy sources have been selected in the past. Specifically, we use the sample from Bouwens et al. (2015), for which multi-wavelength catalogues are available from GREATS (Stefanon et al. 2021b). For consistency, we rederive the photometric redshifts and pdfs for this sample using the same EAZY set-up as for our main selection. We then select the groups of sources with best-fitting redshifts at $7 \leq z \leq 8$ and $8 \leq z \leq 9$. From these, we limit the sources at $H_{160} = 27.7$ mag, which corresponds to the 5σ detection limit in our EGS data around the LAEs.

To get a histogram of expected sources in an area equivalent to a single WFC3/IR pointing, we divide the GOODS-S and GOODS-N fields into circular cells with radius 1.2 arcmin, corresponding to an area of 4.5 arcmin^2 each, and count the number of the selected sources within each cell. The positioning of the cells was chosen on a grid allowing for a small (< 10 per cent) overlap between different areas. In total, the GOODS-S field was thus split into 42 independent regions, while the GOODS-N field was divided into 40 separate cells.

The number count histograms of these 82 regions are also shown in Fig. 2. The average number of sources per cell is 1.2 at $z \sim 7-8$ and 0.45 at $z \sim 8-9$, which is consistent with the average expected number from the UV LF derived in the previous section. However, the empirical histograms further allow us to visualize the effect of cosmic variance. For example, out of 82 independent cells in both GOODS fields, none contain eight sources, while only two contain ≥ 5 $z \sim 7-8$ galaxies. Empirically, finding ≥ 5 galaxies is thus expected only with a 2.4 per cent probability.

At higher redshift, the largest number of galaxies in a given 4.5 arcmin^2 region is three. Based on this, our finding of four (five to eight) sources around the UV luminous LAEs at $z > 8$ ($z = 7-8$) clearly indicates that these galaxies live in early overdensities. We quantify this in more detail in the next section.

4.2 Prevalent overdensities around UV luminous galaxies

We now evaluate the environment of the *HST* fields around the UV luminous sources. We start with the two Ly α sources at $z \sim 7.5$, around which we find five and eight sources in 4.5 arcmin^2 . This is $3 \times$ and $5 \times$ overdense relative to the expected number of 1.57 sources based on the UV LF.

In order to compute more accurate probabilities to find five or eight sources when 1.57 are expected we specifically account for cosmic variance. To do this, we use the publicly available cosmic variance calculator `galcv2` of Trapp & Furlanetto (2020). For a 4.5 arcmin^2 field and a depth of $\Delta z = 1$, this predicts a relative σ_{CV} of 32 per cent at $z = 7.5$ and 38 per cent at $z = 8.5$, down to our magnitude limits. These numbers are similar (albeit somewhat smaller) than the predicted cosmic variance from Trenti & Stiavelli (2008).

The full probabilities are then derived from a Monte Carlo simulation in which we first perturb the expected numbers of galaxies from the UV LF by the relative cosmic variance and then draw from the Poisson distribution. Doing this, we find that the probability to

²<https://github.com/adamtrapp/galcv>

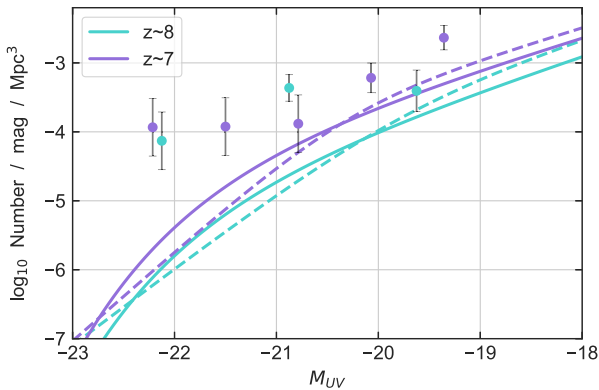


Figure 3. UV luminosity functions in the EGS field centred around the four UV-luminous sources (dots) compared to expected average Schechter LFs as derived in Bouwens et al. (2021, solid lines), and double power-law LFs (Bowler et al. 2020, dashed lines). The purple curve shows the LFs for the $z = 7-8$ galaxies, while the cyan line corresponds to $z = 8-9$. This analysis shows that these UV luminous sources lie in areas with a general density enhancement of $3-9 \times$ that extends to fainter galaxies.

find eight sources, when 1.57 are expected is indeed small with 0.08 per cent. This corresponds to a 3.2σ result. Similarly, the probability to find ≥ 5 galaxies is only 3.1 per cent, consistent with our empirical estimate above. This still represents a significance of 1.9σ .

For the higher redshift fields, we find four sources in each pointing, while only 0.46 were expected on average. This corresponds to an enhancement of $8.7\times$. Doing the same calculation as above, we find that the probability of finding four (or more) sources is only 0.2 per cent, corresponding to a 2.9σ result for each field separately. These calculations show that overdensities around UV luminous sources have been significantly detected in all four cases, with overdensity values in the range $3-9\times$.

This excess can also be seen when looking at the UV LF derived in our target fields alone. Fig. 3 shows these UV LFs at $z = 7-8$ and $z = 8-9$ as derived from the two WFC3/IR pointings centred at the respective redshifts. To compute this, we use the same selection functions as derived in Section 4.1.1 and compute the effective volume in a given magnitude bin. Given the small area (of 9 arcmin^2) centred on UV luminous galaxies, the UV LF in these fields is significantly enhanced in the brightest bins (with $M_{UV} \sim -22$). However, as can be seen, at the fainter end these UV LFs continue to lie significantly above the expected field average values. This is consistent with the hypothesis that these UV luminous galaxies lie in overdensities that are generally enhanced relative to the rest of the Universe. Our results thus indicate that the most UV luminous sources can indeed be used to pinpoint the first overdense regions in the early Universe.

4.3 Possible impact of low-redshift contamination

In Section 3, we outlined our selection criteria that require high-redshift probabilities of $\mathcal{P}(6 \leq z \leq 9) \geq 50$ per cent for the sources around EGS-zs8-1 and -2 and $\mathcal{P}(z \geq 7) \geq 50$ per cent for the sources around EGSY-z8p7 and EGS910-3. This means that there is a chance for a few of the sources to actually lie at lower redshifts, which could impact our overdensity estimates. Here, we thus discuss how our results would change if we had used stricter selection criteria, namely more than 80 per cent high-redshift probabilities, rather than 50 per cent. In that case, we still select four neighbouring sources within 4.5 arcmin^2 around EGS-zs8-1, two galaxies around EGS-zs8-

2, two sources around EGSY-z8p7, and two sources around EGS910-3. Hence, these fields remain overdense, albeit with slightly reduced overdensity factors: $1.98_{-0.93}^{+1.51}$, $1.16_{-0.67}^{+1.02}$, $4.26_{-2.21}^{+3.97}$, and $4.26_{-2.21}^{+3.97}$, respectively.

The probabilities of finding such fainter sources around the luminous central ones, similarly remain high. We find two neighbouring sources around EGSY-z8p7 and EGS910-3, while only 0.46 were expected on average. The probability of finding three (or more) sources is thus still only 1.5 per cent, corresponding to a 2.44σ result for each field separately. In the lower redshift fields, we would find four and two sources around EGS-zs8-1 and -2, respectively, while 1.57 were expected. The probability to find five sources when 1.57 are expected is 3.1 per cent, which corresponds to a 2.2σ result. Similarly, the probability to find three sources when 1.57 are expected is 21.8 per cent, which corresponds to a 1.23σ result. This shows that our conclusions regarding prevalent overdensities around UV luminous galaxies remains unaffected even if a stricter candidate selection is used.

5 EXPECTATIONS FROM SIMULATIONS

In this section, we discuss what simulations predict for the environment of UV luminous galaxies similar to those we have observed.

Specifically, Qin et al. (2022) studied the environment of $z = 8$ galaxies in the MERAXES semi-analytical model (Mutch et al. 2016; Qin et al. 2017) as part of the DRAGONS simulation program (Poole et al. 2016).

5.1 Number of neighbouring galaxies

Qin et al. (2022) predicted that the most luminous galaxies preferentially lie in overdense regions, in agreement with what we find here from observations. In particular, Qin et al. (2022) used their simulations to compute the number of expected sources within a WFC3/IR field of view. This can be directly compared to our observational data.

Fig. 4 shows the cumulative number of galaxies expected around the eight most luminous central sources (having $M_{UV} < -21.5$) in the simulations down to the same magnitude limit as used in our observations. As can be seen, the cumulative number varies between 3 and 13 sources, with a median of 8.5. This is in excellent agreement with our findings around the two sources EGS-zs8-1 and EGS-zs8-2. Both the simulations and the observations thus find a boost in the number counts around luminous sources compared to the field by $\sim 3-5\times$.

5.2 Ionized bubble sizes

The MERAXES simulation further allows us to measure the radii of the ionized bubbles around galaxies. Qin et al. (2022) show that the most luminous sources sit in some of the largest ionized bubbles, resulting in a higher total transmission of the Ly α emission line (see also Wyithe & Loeb 2005; Geil et al. 2017; Hutter et al. 2017). The most luminous simulated central sources lie in ionized regions with measured radii of around 8–9 comoving Mpc, corresponding to ~ 1 physical Mpc at these redshifts (see Fig. 5). We can thus expect similar ionized region sizes around our observed galaxies. Using simple estimates, this is indeed what we infer as discussed below.

To convincingly conclude that all of the associated sources we find for our sample lie within the respective ionized bubbles would require both spectroscopic confirmation of the association and, ideally, the presence of Lyman alpha emission. None the less, using the same approach as in Matthee et al. (2018) we can estimate the sizes of

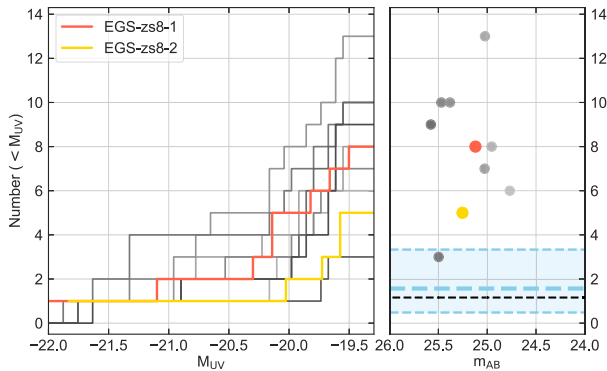


Figure 4. The cumulative number of the sources within an area of 4.5 arcmin^2 at $z \sim 8$, both in simulation and in our observations. The left-hand panel shows the cumulative numbers as a function of absolute magnitude. The coloured lines correspond to the actual numbers of galaxies that we have identified in the *HST* data in different fields (orange for EGS-zs8-1; yellow for EGS-zs8-2). The grey lines indicate the number of galaxies which were selected in the same way in the DRAGONS simulation around luminous central galaxies (Qin et al. 2022). The right-hand panel shows the total number of sources as a function of the magnitude of the brightest source selected down to our 27.7 mag limit using the same colours as for the cumulative histograms. The blue line corresponds to the expected number based on the UV LF and our selection function (same as Fig. 2), with the shaded blue region showing the 16th to 84th percentile. The horizontal black dashed line shows the average number of sources in the GOODS fields within the same area. Both the simulations and the observations thus find a boost of $\sim 3\text{--}5 \times$ in the number of galaxies around the most luminous sources.

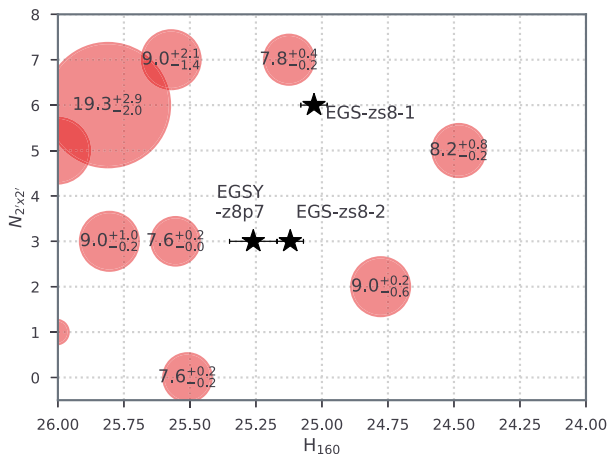


Figure 5. Number of neighbouring galaxies brighter than $H_{160} = 27.5$ mag for EGS-zs8-1, EGS-zs8-2, and EGSY-z8p7 (see the star symbols) as a function of their UV magnitudes. Theoretical expectation using the DRAGONS simulation (see more in e.g. fig. 2 of Qin et al. 2022) is shown with circles for comparison. The size of the corresponding H II bubbles (in units of cMpc; indicated by varying circle sizes) is shown with the uncertainties drawn from 500 mock observations.

the ionized bubbles that each of our sources individually could carve out of the neutral IGM. Assuming a spherical shape of the ionized regions around the galaxies, the expected radii range from 0.5 up to 1.1 pMpc. These results are consistent with previous estimates in the literature for possible bubble sizes at these redshifts (see e.g. Castellano et al. 2018; Tilvi et al. 2020; Endsley et al. 2021b).

While Tilvi et al. (2020) have confirmed the physical association of two sources around EGS-zs8-1 through spectroscopy, the new galaxies identified in this paper only have photometric redshifts available

at the moment. The respective uncertainties in 3D distances are thus too large to determine the physical associations of these galaxies with the central UV luminous targets. However, our detection of an enhancement of fainter galaxies around all these sources points at a larger scale overdensity in the EGS field (see also Bouwens et al. 2015, 2019; Finkelstein et al. 2022).

Interestingly, the two UV luminous LAEs EGS-zs8-1 and EGS-zs8-2 are only separated by 9.1 pMpc from each other. It is thus possible that these two sources lie in a larger, ionized region that spans from $z = 7.5$ to $z = 7.7$. Future observations, e.g. with *JWST* spectroscopy will be needed to confirm this.

6 SUMMARY AND CONCLUSIONS

In this paper, we identified faint sources at $z > 7$ around three confirmed UV luminous LAEs and another, nearby $z_{\text{phot}} \sim 9$ target in the CANDELS/EGS field. We presented dedicated *HST* data and combined this with ancillary *HST* and Spitzer/IRAC imaging in this field.

We find a significant enhancement of fainter galaxies within a WFC3/IR pointing of 4.5 arcmin^2 around each of these UV luminous, central sources. By comparing the number of detected galaxy candidates with the expected numbers from the UV LFs at these redshifts and with the numbers in the two GOODS fields, we estimate these areas to be enhanced by $3\text{--}9 \times$ compared to the average field.

Our observational findings are in excellent agreement with the predictions from the MERAXES simulation (Qin et al. 2022), which also find a boost in fainter neighbouring sources around UV luminous galaxies. In these simulations, the combined ionizing photon output of the ensemble of galaxies around the central sources produce ionized regions with radii of ~ 1 pMpc, allowing Ly α photons to be transmitted even when the surrounding IGM is still highly neutral.

Combined with these simulation results, our observational finding of overdense regions around these luminous $z = 7.5\text{--}8.7$ LAEs thus strongly suggest that the local galaxy environment plays a driving role in the Ly α transmission. Specifically, the field around EGSY-z8p7 at $z_{\text{spec}} = 8.683$ is overdense by a factor $\sim 8.7 \times$, suggesting that this source might sit in one of the first overdensities and ionized bubbles in the Universe, only ~ 500 Myr after the big bang.

The crucial next step is to obtain spectroscopic redshifts for these overdensities in order to map out their 3D structure and estimate the size of the overall ionized regions. The approved *JWST* cycle 1 program GO-2279 (Naidu et al. 2021) will achieve exactly this based on NIRCcam/grism observations of EGSY-z8p7 and EGS910-3, which is only separated by 3.7 arcmin. These observations will provide a sample of [O III]5007 emission line selected sources at $z = 7\text{--}9$, and will thus significantly improve the overdensity measurement. Other NIRCcam/grism and NIRSpc observations over other fields are poised to identify a large number of ionized bubbles in the EoR in the near future. This will further clarify the importance of other possible origins for enhanced Ly α transmission from UV luminous galaxies, such as velocity offsets or very hard and strong ionization fields, e.g. from an AGN contribution.

The fact that we find an overdensity around each of the three UV luminous Ly α emitting galaxies only based on photometric redshifts strongly suggests that the Ly α transmission is intimately connected to the overall galaxy environment that helps to create ionized regions. Turning this around, these UV luminous, early LAEs can be used to pinpoint the earliest overdense regions in the Universe, where star-formation and reionization first started. This will become particularly interesting with the availability of larger samples of UV luminous

LBGs and LAEs from future wide-area surveys with the Euclid or Roman Space Telescopes and follow-up spectroscopy.

ACKNOWLEDGEMENTS

We would like to thank the referee for their insightful comments that have helped clarify and improve this manuscript. We acknowledge support from the Swiss National Science Foundation through the SNSF Professorship grant 190079 (PAO, JK). The Cosmic Dawn Center (DAWN) is funded by the Danish National Research Foundation under grant No. 140. This research was supported by the Australian Research Council Centre of Excellence for All Sky Astrophysics in 3 Dimensions (ASTRO 3D), through project number CE170100013. Part of this work was performed on the OzSTAR national facility at Swinburne University of Technology, which is funded by Swinburne University of Technology and the National Collaborative Research Infrastructure Strategy (NCRIS). ST is supported by the 2021 Research Fund 1.210134.01 of UNIST (Ulsan National Institute of Science & Technology). RSE acknowledges funding from the European Research Council (ERC) under the European Union's Horizon 2020 research and innovation programme (grant agreement No 669253). RJB and MS acknowledge support from TOP grant TOP1.16.057. RS acknowledges support from a STFC Ernest Rutherford Fellowship (ST/S004831/1). AH acknowledges support from the European Research Council's starting grant ERC StG-717001 (DELPHI). AZ acknowledges support by Grant No. 2020750 from the United States-Israel Binational Science Foundation (BSF) and Grant No. 2109066 from the United States National Science Foundation (NSF), and by the Ministry of Science and Technology, Israel.

DATA AVAILABILITY

The *HST* data underlying this article will be publicly released as High-Level Science Product (HLSP) as part of the Hubble Legacy Fields (HLF) project (Illingworth et al. 2016; Whitaker et al. 2019). A pre-release version can be shared on reasonable request to the corresponding author.

REFERENCES

Anders P., Fritze-v. Alvensleben U., 2003, *A&A*, 401, 1063
 Ashby M. L. N. et al., 2015, *ApJS*, 218, 33
 Barkana R., Loeb A., 2004, *ApJ*, 609, 474
 Barmby P., Huang J. S., Ashby M. L. N., Eisenhardt P. R. M., Fazio G. G., Willner S. P., Wright E. L., 2008, *ApJS*, 177, 431
 Bertin E., Arnouts S., 1996, *A&AS*, 117, 393
 Bielby R. et al., 2012, *A&A*, 545, A23
 Bosman S. E. I. et al., 2022, *MNRAS*, 514, 55
 Bouwens R. J. et al., 2015, *ApJ*, 803, 34
 Bouwens R. J. et al., 2016, *ApJ*, 830, 67
 Bouwens R. J., Stefanon M., Oesch P. A., Illingworth G. D., Nanayakkara T., Roberts-Borsani G., Labbé I., Smit R., 2019, *ApJ*, 880, 25
 Bouwens R. J. et al., 2021, *AJ*, 162, 47
 Bowler R. A. A., Jarvis M. J., Dunlop J. S., McLure R. J., McLeod D. J., Adams N. J., Milvang-Jensen B., McCracken H. J., 2020, *MNRAS*, 493, 2059
 Brammer G. B., van Dokkum P. G., Coppi P., 2008, *ApJ*, 686, 1503
 Bruzual G., Charlot S., 2003, *MNRAS*, 344, 1000
 Calzetti D., Armus L., Bohlin R. C., Kinney A. L., Koornneef J., Storchi-Bergmann T., 2000, *ApJ*, 533, 682
 Castellano M. et al., 2016, *ApJ*, 818, L3
 Castellano M. et al., 2018, *ApJ*, 863, L3
 Castellano M. et al., 2022, *A&A*, 662, A115

Dayal P., Ferrara A., Saro A., Salvaterra R., Borgani S., Tornatore L., 2009, *MNRAS*, 400, 2000
 Dayal P., Maselli A., Ferrara A., 2011, *MNRAS*, 410, 830
 De Barros S., 2017, Beacons in the Dark: Using the Most Distant Galaxies to Probe Cosmic Reionization. HST Proposal 15103
 De Barros S., Oesch P. A., Labbé I., Stefanon M., González V., Smit R., Bouwens R. J., Illingworth G. D., 2019, *MNRAS*, 489, 2355
 Endsley R., Stark D. P., Chevallard J., Charlot S., 2021a, *MNRAS*, 500, 5229
 Endsley R., Stark D. P., Charlot S., Chevallard J., Robertson B., Bouwens R. J., Stefanon M., 2021b, *MNRAS*, 502, 6044
 Erb D. K. et al., 2014, *ApJ*, 795, 33
 Euclid Collaboration, 2022, *A&A*, 658, A126
 Finkelstein S. L. et al., 2022, *ApJ*, 928, 52
 Fontana A. et al., 2010, *ApJ*, 725, L205
 Geil P. M., Mutch S. J., Poole G. B., Duffy A. R., Mesinger A., Wyithe J. S. B., 2017, *MNRAS*, 472, 1324
 Greig B., Mesinger A., 2017, *MNRAS*, 465, 4838
 Grogan N. A. et al., 2011, *ApJS*, 197, 35
 Gronke M. et al., 2021, *MNRAS*, 508, 3697
 Hashimoto T. et al., 2018, *Nature*, 557, 392
 Hashimoto T. et al., 2019, *PASJ*, 71, 71
 Hoag A. et al., 2019, *ApJ*, 878, 12
 Hu W. et al., 2021, *Nat. Astron.*, 5, 485
 Hutter A., Dayal P., Müller V., Trott C. M., 2017, *ApJ*, 836, 176
 Iliiev I. T., Mellema G., Pen U. L., Merz H., Shapiro P. R., Alvarez M. A., 2006, *MNRAS*, 369, 1625
 Illingworth G. et al., 2016, preprint (arXiv:1606.00841)
 Ishigaki M., Ouchi M., Harikane Y., 2016, *ApJ*, 822, 5
 Jiang L. et al., 2021, *Nat. Astron.*, 5, 256
 Jung I. et al., 2020, *ApJ*, 904, 144
 Koekemoer A. M. et al., 2011, *ApJS*, 197, 36
 Kulkarni G., Keating L. C., Hachnelt M. G., Bosman S. E. I., Puchwein E., Chardin J., Aubert D., 2019, *MNRAS*, 485, L24
 Labbé I. et al., 2013, *ApJ*, 777, L19
 Labbé I. et al., 2015, *ApJS*, 221, 23
 Laporte N., Nakajima K., Ellis R. S., Zitrin A., Stark D. P., Mainali R., Roberts-Borsani G. W., 2017, *ApJ*, 851, 40
 Laporte N., Meyer R. A., Ellis R. S., Robertson B. E., Chisholm J., Roberts-Borsani G. W., 2021, *MNRAS*, 505, 3336
 Larson R. L. et al., 2022, *ApJ*, 930, 104
 Madau P., 1995, *ApJ*, 441, 18
 Mainali R. et al., 2018, *MNRAS*, 479, 1180
 Mason C. A. et al., 2018, *ApJ*, 857, L11
 Matthee J., Sobral D., Gronke M., Paulino-Afonso A., Stefanon M., Röttgering H., 2018, *A&A*, 619, A136
 Matthee J., Sobral D., Gronke M., Pezzulli G., Cantalupo S., Röttgering H., Darvish B., Santos S., 2020, *MNRAS*, 492, 1778
 McQuinn M., Lidz A., Zahn O., Dutta S., Hernquist L., Zaldarriaga M., 2007, *MNRAS*, 377, 1043
 Miralda-Escudé J., 1998, *ApJ*, 501, 15
 Momcheva I. G. et al., 2016, *ApJS*, 225, 27
 Mutch S. J., Geil P. M., Poole G. B., Angel P. W., Duffy A. R., Mesinger A., Wyithe J. S. B., 2016, *MNRAS*, 462, 250
 Naidu R. P., Tacchella S., Mason C. A., Bose S., Oesch P. A., Conroy C., 2020, *ApJ*, 892, 109
 Naidu R. et al., 2021, Where Cosmic Dawn Breaks First: Mapping the Primordial Overdensity Powering a z 9 Ionized Bubble. JWST Proposal. Cycle 1
 Ocvirk P. et al., 2020, *MNRAS*, 496, 4087
 Oesch P. A. et al., 2015, *ApJ*, 804, L30
 Oesch P. A. et al., 2016, *ApJ*, 819, 129
 Ono Y., 2012, in Umemura M., Omukai K., eds, AIP Conf. Ser. Vol. 1480, First Stars IV - from Hayashi to the Future. Am. Inst. Phys., New York, p. 277
 Ouchi M., Ono Y., Shibuya T., 2020, *ARA&A*, 58, 617
 Pentericci L. et al., 2011, *ApJ*, 743, 132
 Pentericci L. et al., 2014, *ApJ*, 793, 113
 Pentericci L. et al., 2018, *A&A*, 619, A147

- Planck Collaboration VI, 2020, *A&A*, 641, A6
- Poole G. B., Angel P. W., Mutch S. J., Power C., Duffy A. R., Geil P. M., Mesinger A., Wyithe S. B., 2016, *MNRAS*, 459, 3025
- Qin Y. et al., 2017, *MNRAS*, 472, 2009
- Qin Y., Wyithe J. S. B., Oesch P. A., Illingworth G. D., Leonova E., Mutch S. J., Naidu R. P., 2022, *MNRAS*, 510, 3858
- Roberts-Borsani G. W. et al., 2016, *ApJ*, 823, 143
- Robertson B. E., 2021, preprint (arXiv:2110.13160)
- Schenker M. A., Stark D. P., Ellis R. S., Robertson B. E., Dunlop J. S., McLure R. J., Kneib J.-P., Richard J., 2012, *ApJ*, 744, 179
- Skelton R. E. et al., 2014, *ApJS*, 214, 24
- Smit R. et al., 2015, *ApJ*, 801, 122
- Smith A., Kannan R., Garaldi E., Vogelsberger M., Pakmor R., Springel V., Hernquist L., 2022, *MNRAS*, 512, 3243
- Stark D. P., Ellis R. S., Chiu K., Ouchi M., Bunker A., 2010, *MNRAS*, 408, 1628
- Stark D. P. et al., 2017, *MNRAS*, 464, 469
- Stefanon M. et al., 2017, *ApJS*, 229, 32
- Stefanon M., Bouwens R. J., Labbé I., Illingworth G. D., Gonzalez V., Oesch P. A., 2021a, *ApJ*, 922, 29
- Stefanon M. et al., 2021b, *ApJS*, preprint (arXiv:2110.06226)
- Tilvi V. et al., 2016, *ApJ*, 827, L14
- Tilvi V. et al., 2020, *ApJ*, 891, L10
- Trapp A. C., Furlanetto S. R., 2020, *MNRAS*, 499, 2401
- Trenti M., Stiavelli M., 2008, *ApJ*, 676, 767
- Trenti M. et al., 2012, *ApJ*, 746, 55
- Treu T., Schmidt K. B., Trenti M., Bradley L. D., Stiavelli M., 2013, *ApJ*, 775, L29

- Whitaker K. E. et al., 2019, *ApJS*, 244, 16
- Wilkins S. M., Stanway E. R., Bremer M. N., 2014, *MNRAS*, 439, 1038
- Willott C. J., Carilli C. L., Wagg J., Wang R., 2015, *ApJ*, 807, 180
- Wyithe J. S. B., Loeb A., 2005, *ApJ*, 625, 1
- Zitrin A. et al., 2015, *ApJ*, 810, L12

APPENDIX: STAMPS AND PHOTOMETRIC REDSHIFT LIKELIHOODS FOR THE HIGH-Z SAMPLE

Here, we show the image stamps, SEDs, and photometric redshift likelihood functions for all sources that were selected in our fields. In A1, we show how our photometric redshifts compare to the spectroscopic redshifts measured for the UV-luminous central targets. The neighbouring sources around the four central targets are shown in Figs A2, A3, A4, and A5. While there is clearly a relatively large spread, the combined likelihood functions for the neighbours agree well with the redshifts of the central sources, indicating that the majority of our selected galaxies indeed have a good chance to be physically associated with the central UV-luminous sources. Spectroscopy will be needed to confirm this in the future, however.

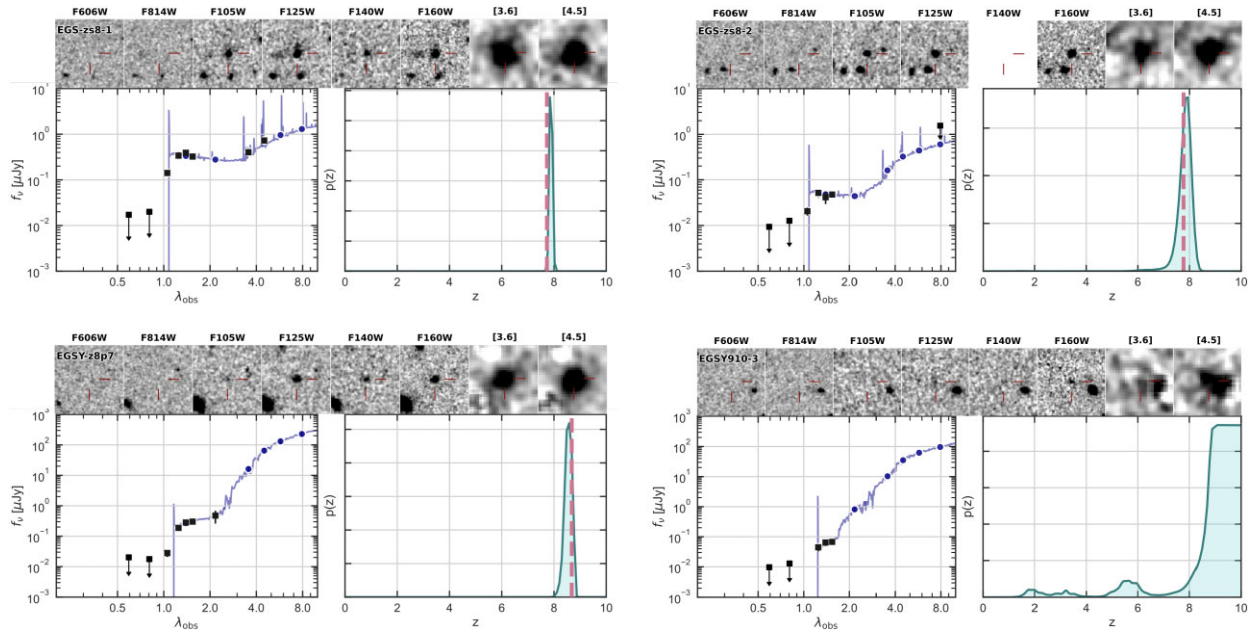


Figure A1. Multiwavelength images and SEDs of the UV-luminous central targets: three LAEs and EGS910-3. For each source, the top panels show, from left to right, *HST*/ACS V_{606} , I_{814} , *HST*/WFC3 Y_{105} , J_{125} , H_{160} , and Spitzer/IRAC 3.6 and 4.5 μm stamps. The stamps are centred on the candidate galaxies, whose positions are further indicated by two red lines. The lower panels show the SED (purple curve with uncertainties), the photometry (black squares with uncertainties), and the resulting probability distribution of redshift $\mathcal{P}(z)$ (green curve). The pink vertical lines represent the spectroscopic redshift of the LAEs, showing that the photometric redshifts are accurate for these sources. The last source, EGS910-3, does not have a spectroscopic redshift measurement yet. Our photometric redshift is in excellent agreement with the original determination of Bouwens et al. (2016).

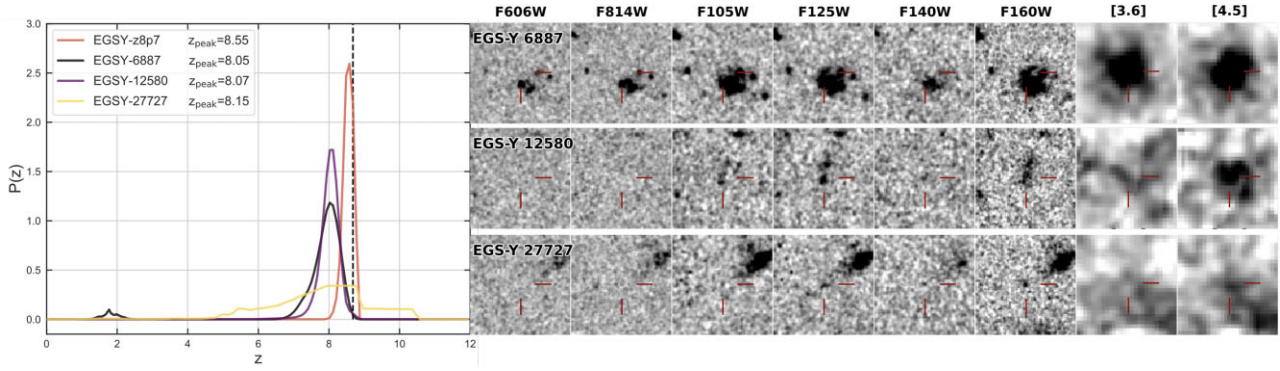


Figure A2. Redshift pdfs $\mathcal{P}(z)$ and stamps of fainter $z_{\text{phot}} > 8$ sources in the pointing around EGSY-z8p7. The $\mathcal{P}(z)$ of the UV luminous central target is also shown (orange line), indicating that the neighbouring sources have a significant probability to be physically associated with the central source. The stamps show the same filters as A1 and are labelled on the top.

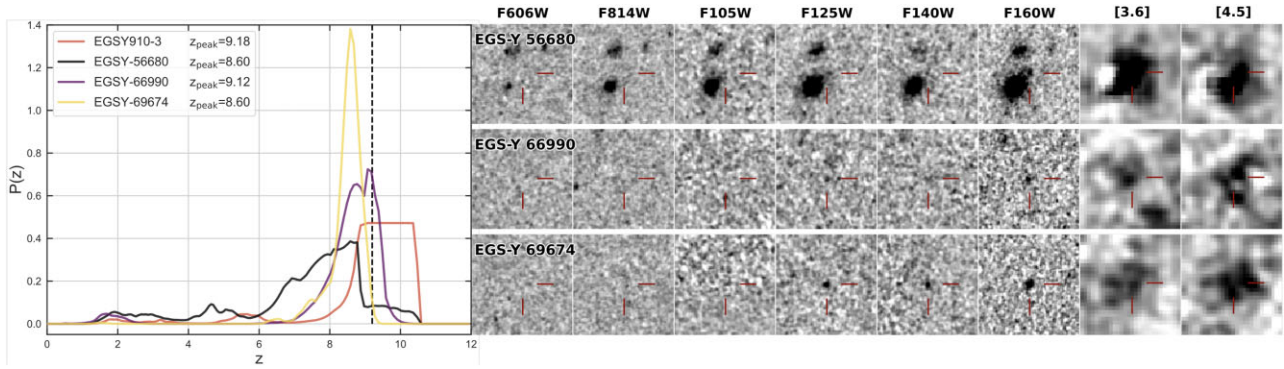


Figure A3. The same as Fig. A2 for the neighbouring sources around EGS910-3 with $z_{\text{phot}} > 8$.

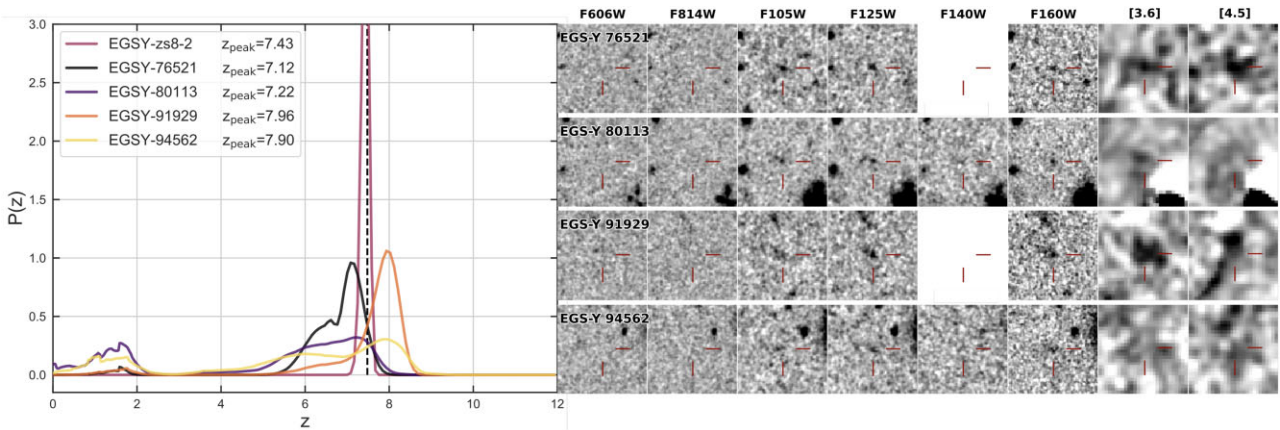


Figure A4. The same as Fig. A2 for the neighbouring sources around EGS-zs8-2 with $z_{\text{phot}} = 7-8$.

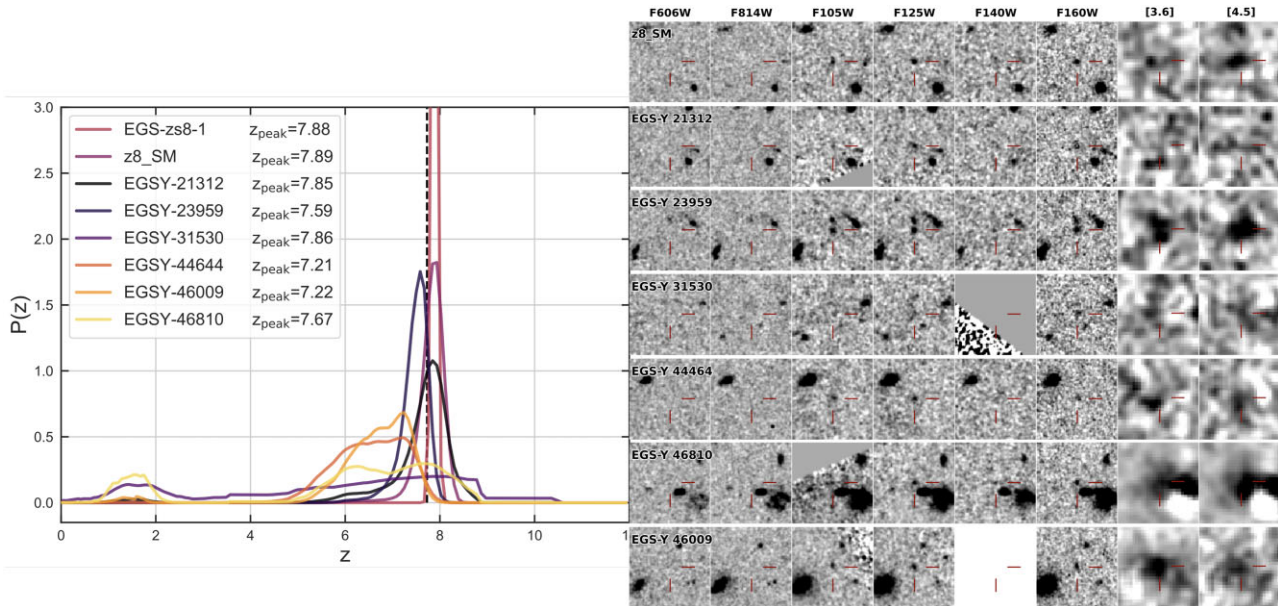


Figure A5. The same as Fig. A2 for the neighbouring sources around EGS-zs8-1 with $z_{\text{phot}} = 7-8$.

¹Department of Astronomy, University of Geneva, Chemin Pegasi 51, CH-1290 Versoix, Switzerland

²GRAPPA, Anton Pannekoek Institute for Astronomy and Institute of High-Energy Physics, University of Amsterdam, Science Park 904, NL-1098 XH Amsterdam, the Netherlands

³Nikhef, Science Park 105, NL-1098 XG Amsterdam, the Netherlands

⁴Cosmic Dawn Center (DAWN), Niels Bohr Institute, University of Copenhagen, Jagtvej 128, København N, DK-2200, Denmark

⁵School of Physics, University of Melbourne, Parkville, VIC 3010, Australia

⁶ARC Centre of Excellence for All Sky Astrophysics in 3 Dimensions (ASTRO 3D)

⁷Scuola Normale Superiore, Piazza dei Cavalieri 7, I-56126 Pisa, Italy

⁸Center for Astrophysics | Harvard & Smithsonian, 60 Garden Street, Cambridge, MA 02138, USA

⁹Leiden Observatory, Leiden University, PO Box 9500, NL-2300 RA Leiden, the Netherlands

¹⁰Department of Physics and Astronomy, University College London, Gower Street, London WC1E 6BT, UK

¹¹Steward Observatory, University of Arizona, 933 N Cherry Ave, Tucson, AZ 85721, USA

¹²Kapteyn Astronomical Institute, University of Groningen, PO Box 800, NL-9700 AV Groningen, the Netherlands

¹³Department of Astronomy and Astrophysics, UCO/Lick Observatory, University of California, Santa Cruz, CA 95064, USA

¹⁴Centre for Astrophysics & Supercomputing, Swinburne University of Technology, PO Box 218, Hawthorn, VIC 3112, Australia

¹⁵Kavli Institute for Cosmology, University of Cambridge, Madingley Road, Cambridge CB3 0HA, UK

¹⁶Cavendish Laboratory, University of Cambridge, 19 JJ Thomson Avenue, Cambridge CB3 0HE, UK

¹⁷Department of Physics and Astronomy, University of California, Los Angeles, 430 Portola Plaza, Los Angeles, CA 90095, USA

¹⁸Astrophysics Research Institute, Liverpool John Moores University, 146 Brownlow Hill, Liverpool L3 5RF, UK

¹⁹Department of Physics, Ulsan National Institute of Science and Technology (UNIST), Ulsan 44919, Republic of Korea

²⁰Physics Department, Ben-Gurion University of the Negev, PO Box 653, Be'er-Sheva 84105, Israel

This paper has been typeset from a $\text{\TeX}/\text{\LaTeX}$ file prepared by the author.